2017

An Experimental Method for Controlled Generation and Characterization of Microchannel Slug Flow Boiling

T A. Kingston
Purdue University

J A. Weibel
Purdue University, jaweibel@purdue.edu

S V. Garimella
Purdue University, sureshg@purdue.edu

Kingston, T A.; Weibel, J A.; and Garimella, S V., "An Experimental Method for Controlled Generation and Characterization of Microchannel Slug Flow Boiling" (2017). *CTRC Research Publications.* Paper 310.
http://dx.doi.org/10.1016/j.ijheatmasstransfer.2016.09.036

An Experimental Method for Controlled Generation and Characterization of Microchannel Slug Flow Boiling[1]

Todd A. Kingston, Justin A. Weibel, and Suresh V. Garimella[2]

Cooling Technologies Research Center, an NSF I/UCRC

School of Mechanical Engineering, Purdue University, West Lafayette, Indiana 47907 USA

Abstract

This study uses high-speed imaging to characterize microchannel slug flow boiling using a novel experimental test facility that generates an archetypal flow regime suitable for high-fidelity characterization of key hydrodynamic and heat transfer parameters. Vapor and liquid phases of the fluorinated dielectric fluid HFE-7100 are independently injected into a T-junction to create a saturated two-phase slug flow, thereby eliminating the flow instabilities and flow-regime transitions that would otherwise result from stochastic generation of vapor bubbles by nucleation from a superheated channel wall. Slug flow boiling is characterized in a heated, 500 μm-diameter borosilicate glass microchannel. A thin layer of optically transparent and electrically conductive indium tin oxide coated on the outside surface of the microchannel provides a uniform heat flux via Joule heating. High-speed flow visualization images are analyzed to quantify the uniformity of the vapor bubbles and liquid slugs generated, as well as the growth of vapor bubbles under heat fluxes ranging from 30 W/m^2 to 5160 W/m^2. A method is demonstrated for measuring liquid film thickness from the visualizations using a ray-tracing

[1] Submitted for review to the *International Journal of Heat and Mass Transfer*

[2] Corresponding author: sureshg@purdue.edu

procedure to correct for optical distortions. Characterization of the slug flow boiling regime that is generated demonstrates the unique ability of the facility to precisely control and quantify hydrodynamic and heat transfer characteristics. The experimental approach demonstrated in this study provides a unique platform for the investigation of microchannel slug flow boiling transport under controlled, stable conditions suitable for model validation.

Keywords: flow boiling, heat transfer, microchannel, slug flow, two-phase flow, vapor bubbles

Nomenclature

A_s	inside surface area of the microchannel
Bo	Bond number $[(\rho_l-\rho_v)gD^2/\sigma_l]$
D	microchannel diameter
D_b	vapor bubble diameter
g	gravitational acceleration constant
L_b	vapor bubble length
L_m	microchannel length
L_s	liquid slug length
L_0	initial vapor bubble/liquid slug length
P_{in}	input power
P_{loss}	power loss
P_{total}	total power
q''	heat flux
Re_D	Reynolds number (V_bD/v_l)
t_w	microchannel wall thickness
V_b	vapor bubble velocity
x	transverse position relative to microchannel centerline
y	axial position relative to T-junction center
y'	axial position relative to camera field of view
z	vertical position relative to microchannel centerline

Greek Letters

δ	liquid film thickness
θ	angle between normal and incident/refracted light
v_l	liquid kinematic viscosity
ρ_l	liquid density
ρ_v	vapor density
σ_l	liquid surface tension

1 Introduction

Two-phase flows are commonly encountered in nuclear, power generation, petroleum, and other industries. In general, two-phase flows can be classified according to whether phase change is occurring, which leads to strong differences in the underlying physics. Flows not undergoing phase change involve two different immiscible chemical components, and are sometimes referred to as two-component, two-phase flows (*e.g.*, nitrogen-water flow) [1]. Phase-change flows contain a single component but comprise two different phases separated by an interface; steam-water flow is an example of a single-component, two-phase flow. Phase-change flows can be either condensing (flow condensation) or evaporating (flow boiling).

Slug flow is one of the most common two-phase flow regimes in applications at the microscale [2-5], ranging from lab-on-a-chip devices in medical and pharmaceutical industries [2] to microchannel flow boiling heat sinks for electronics cooling [6, 7]. The slug flow boiling regime, schematically illustrated in Fig. 1, is characterized by elongated vapor bubbles that are circumferentially confined and partitioned in the streamwise direction by liquid slugs. A thin liquid film separates the vapor bubbles from the channel wall; evaporation in this thin liquid film has been shown to be the dominant heat transfer mechanism in slug flow boiling [8]. During flow boiling in microchannels, nucleation and departure of vapor bubbles from the channel wall almost immediately leads to a slug flow regime for channel sizes below a critical value, due to the influence of surface tension and vapor confinement [9]. As a result, the slug flow regime is observed across a wide range of operating conditions and is of significant interest.

The design and optimization of two-phase microchannel cooling systems will likely be accomplished using a combination of reduced-order mechanistic models and direct numerical simulation of flow boiling. Several mechanistic slug flow boiling models of increasing

complexity have been proposed. Peles *et al.* [10] developed a one-dimensional model featuring distinct liquid and vapor regions partitioned by an evaporating interface. Jacobi and Thome [11] proposed a 'two-zone' model consisting of an evaporating vapor bubble region surrounded circumferentially by a thin liquid film, with successive bubbles partitioned by a liquid slug region. A model for the conduction resistance of the thin liquid film was used to describe the effective evaporative heat transfer coefficient. A 'three-zone' model was presented by Thome *et al.* [8] by including an additional vapor slug region, where no liquid film exists, and a method for prediction of the liquid film thickness. This model was later adapted by Harirchian and Garimella [12] to include a correlation for the liquid film thickness specific to microchannel length scales. While the aforementioned two- and three-zone models were strictly developed for circular microchannels, a 'four-zone' model was developed by Wang *et al.* [13] to account for a partial dryout region resulting from corner effects in microchannels of rectangular cross-section. These modeling efforts have significantly advanced the understanding of the underlying flow boiling physics, such as the realization that thin-film evaporation governs microchannel flow boiling performance (rather than nucleate boiling) and that cyclic variations in the heat transfer coefficient result from the passage of different fluid zones.

Several recent studies have developed multiphase numerical models for flow boiling that account for complex vapor-liquid interfacial transport phenomena [14-18]. For example, Pan *et al.* [17] demonstrated a cost-effective approach for modeling microchannel flow boiling using a volume-of-fluid (VOF) approach coupled with a saturated-interface-volume phase change model and a moving-reference-frame method that suppresses spurious currents [19]. The growth of single, evaporating vapor bubbles flowing in heated microchannels was simulated. While this was an important step toward the ultimate goal of a comprehensive numerical simulation of the

complete flow boiling problem, a continuous stream of vapor bubbles is more representative of two-phase flows and poses additional challenges for modeling due to the hydrodynamic and thermal interaction between successive vapor bubbles [20]. Magnini and Thome [3] computationally investigated the hydrodynamics and heat transfer characteristics of microchannel slug flow under saturated flow boiling conditions using a continuous stream of artificially generated vapor bubbles. The first vapor bubble entering a fully developed liquid-phase flow and temperature profile had a significantly higher evaporation rate relative to successive vapor bubbles due to the large amount of sensible heat available in the superheated liquid regions; time-periodic behavior was observed after approximately five vapor bubbles.

Despite the recent significant advances in modeling, these state-of-the-art techniques are still validated using test problems for which simplistic analytical solutions are available [15, 17, 18, 21, 22], comparison to temporally and spatially averaged transport quantities that can be easily measured experimentally [16], or cross-comparison between the different numerical modeling approaches [17]. There is a clear need for high-fidelity benchmark experimental data that can be used as a common basis for validation of sophisticated flow boiling models.

Two-phase flows are traditionally generated in flow boiling experiments by vapor bubble nucleation from a heated surface. This incipience-based approach gives rise to a streamwise progression of flow regimes, typically transitioning from bubbly to slug to annular flow. Large stochastic hydrodynamic variations, flow instabilities, and the close proximity of successive vapor bubbles that arise from the nucleation process confound the development of a comprehensive database of well-conditioned experimental results that is amenable for use in the validation of flow boiling models.

Recent experimental efforts have explored innovative techniques that control vapor bubble generation by avoiding a reliance on spontaneous nucleation. Bigham and Moghaddam [23] demonstrated active nucleation control from a 300 nm-diameter heated cavity. By varying the amplitude and period of a pulsed square wave, different time-periodic flow regimes ranging from bubbly to slug to annular were realized in a 120 μm-hydraulic diameter microchannel at very low Reynolds numbers. A method for producing the desired two-phase flow characteristics while completely avoiding nucleation has also been proposed. Scammell and Kim [24] fabricated a test facility capable of producing a single vapor bubble of a desired length which was then injected into a liquid vertical upflow in an optically opaque, heated 6 mm macrochannel. There is a need for experimental approaches capable of producing a continuous stream of vapor bubbles that appropriately emulates the physical behavior of slug flow boiling, with successive vapor bubbles separated by liquid slugs. Such an approach would enable characterization of key hydrodynamic and heat transfer parameters under well-defined boundary and flow conditions that are commonly encountered in microchannel heat sinks.

The current study demonstrates an approach for high-fidelity experimental characterization of the hydrodynamics and heat transfer in microchannel slug flow boiling. The test facility developed provides the unique capability of actively controlling and generating a time-periodic microchannel slug flow boiling regime free of flow-regime transitions and flow instabilities. The experimental facility and the procedure for producing the desired archetypal slug flow regime are first described, followed by presentation of the high-speed flow visualization and image-processing approaches. The vapor bubble and liquid slug uniformity and the growth of vapor bubbles subjected to varying heat fluxes are quantitatively characterized using image analysis techniques.

2 Experimental Methods

2.1 Test Facility

A constant-pressure reservoir is employed to deliver separate streams of degassed HFE-7100 vapor and liquid into a T-junction to create a microchannel slug flow. An open-loop system (Fig. 2), driven by the pressure difference between a pressurized reservoir and the ambient, is used to generate the flow. This approach allows controlled, constant flow rates to be achieved even at low flow rates. Vapor is created inside the fixed-volume, stainless steel pressurized reservoir by continuously boiling fluid using a submerged, horizontally mounted cartridge heater. Electrical power is supplied to the cartridge heater using an adjustable direct current (DC) power supply (XG 150-5.6, Sorenson); the heater is connected to a temperature cut-off to detect a low fluid level. The vapor/liquid mixture inside the reservoir is stratified, as illustrated schematically in Fig. 2, enabling vapor and liquid to be separately drawn out of the reservoir. The pressure in the reservoir is adjustable using a two-phase, back-pressure regulator (EB1ULF1, Equilibar). The back-pressure regulator uses a pilot line to regulate the reservoir pressure by continuously relieving the reservoir of vapor in order to maintain the desired pressure.

Single-phase vapor and single-phase liquid are extracted from the reservoir through two separate lines. Condensation is prevented in the vapor lines using adjustable electrical heating jackets, thereby maintaining slightly superheated single-phase vapor. The local superheat is monitored along the vapor delivery line using pressure transducers and T-type thermocouples, including at a location immediately upstream of the T-junction, to an accuracy of ± 0.5 kPa and ± 1 °C, respectively. The vapor flow rate to the T-junction is controlled using an adjustable

vapor control valve. The single-phase liquid flow is controlled and measured using a liquid flow controller (LC-10CCM-D-EPDM, Alicat) to an accuracy of ± 0.2 mL/min. The liquid mass flow rate is determined using the measured volumetric flow rate and density corresponding to the liquid temperature measured by the flow controller. An electrical heating jacket is used to preheat the liquid to the desired temperature immediately upstream of the T-junction; the subcooling at this location is monitored using a pressure transducer and thermocouple. A PEEK T-junction (MT1PK, Valco) with a 500 μm circular bore is used to combine the vapor and liquid fluid streams and create a two-phase flow in the downstream microchannel. The T-junction bore diameter and test section microchannel inside diameter are identical, yielding a smooth flow path for the two-phase flow. The periodic two-phase flow that forms downstream is a result of the oscillatory behavior that temporary blocks the liquid and allows the vapor to flow before switching and allowing liquid to flow while blocking the vapor, an effect experimentally demonstrated by Miyabayashi *et al.* [25].

The circular cross-section test-section microchannel is made of borosilicate glass (CV5070, Vitrocom) with a nominal inside diameter of D = 500 μm and a wall thickness of t_w =100 μm; this microchannel is mounted horizontally. The microchannel length, nondimensionalized by the channel inside diameter, is L_m/D = 200. The outside surface of the microchannel is custom-coated with a nominally 100 nm-thick layer of indium tin oxide (ITO) using atomic layer deposition (Ultratech Inc.). The ITO layer is optically transparent and electrically conductive, enabling visualization of the two-phase flow while subjected to a uniform Joule heating through the low-thermal conductivity borosilicate glass (1.2 $Wm^{-1}K^{-1}$). Power is supplied to the ITO coating using an adjustable DC power supply (XG 300-2.8, Sorenson). Another PEEK T-junction is used to support the downstream end of the test section

microchannel. The ITO layer is electrically isolated from the flow loop using non-conductive PTFE ferrules and PEEK nuts attached at both ends to the PEEK T-junctions. The pressure drop across the upstream and downstream T-junctions and microchannel is taken as the difference between the measured liquid/vapor pressure immediately upstream of the mixing T-junction and that measured at the downstream T-junction. Fluid leaving the test section (and also the fluid leaving the back-pressure regulator) is collected and passed through a fluid-to-air heat exchanger to condense any vapor before discharging the liquid to an open reservoir at ambient pressure.

All test facility sensor data are obtained at 0.33 Hz using a data acquisition unit (34970A, Agilent) with a 20-channel multiplexer module (34901A, Agilent) using a Labview interface. Power supplied to the test section is quantified by measuring the voltage drop across and current through the ITO microchannel coating; the current is measured using a shunt resistor (6142-1-1000, Empro Shunts). The entire experimental facility is mounted on an isolated optical table (VIS3672-PG2-325A, Newport) to ensure that external vibrations are not transmitted to the components.

2.2 Test Procedure

Immediately prior to testing, the HFE-7100 fluid is degassed by vigorously boiling the liquid in the reservoir using the cartridge heater. A Graham condenser (5977-12, Ace Glass Inc.) condenses the vapor back into the reservoir while non-condensable gases are expelled from the system. An auxiliary pumped loop circulates water through the Graham condenser to promote condensation of the vapor and rejects the heat to the ambient environment using a liquid-to-air heat exchanger (4210G10SB-F9, Lytron). While degassing, liquid in the reservoir is

continuously circulated through a 7 μm particulate filter (SS-4TF-7, Swagelok) and an organic filter (12011, Pall Corporation) to remove any containments from the fluid.

Experiments were initiated by boiling the liquid in the reservoir with only the back-pressure regulator line open. Once the reservoir reaches the pilot line pressure, the back-pressure regulator continously relieves fluid from the reservoir to maintain a constant reservoir pressure of 134.2 ± 0.1 kPa; this constant vapor pressure is required to maintain constant fluid flow rates. The reported uncertainties represent the standard deviation of the values measured over the duration of the test.

The liquid delivery line was then opened and the liquid flow controller was set to deliver a volumetric flow rate of 4.06 ± 0.01 mL/min (mass flow rate of 5.68 ± 0.01 kg/min) to the T-junction. The liquid preheater was turned on and adjusted to achieve a liquid inlet temperature of 60.1 ± 0.1 °C. This corresponds to a subcooling of 4.8 °C at the inlet absolute pressure (113.1 ± 0.6 kPa), ensuring that purely single-phase liquid is delivered to the T-junction. After flow in the liquid delivery line reached steady-state conditions, the vapor line heaters were turned on to preheat the vapor lines. Next, the vapor delivery line was opened. The vapor line heating power and vapor flow rate were iteratively adjusted until the desired downstream slug flow regime (vapor bubble lengths of approximately $L_b/D = 5$) were observed in the visualization images at steady-state conditions. These vapor flow conditions were then held fixed for all power inputs to the test section microchannel. In this study, the average temperature of the vapor being delivered to the T-junction was 71.1 ± 0.2 °C. This corresponds to a superheat of 6.9 °C at the inlet absolute pressure (111.1 ± 0.6 kPa), ensuring that purely single-phase vapor is delivered to the T-junction. Note that when the subcooled liquid and superheated vapor combine at the T-junction, some developing length is required before equilibrium is reached and a saturated two-

phase flow is established. The vapor superheat and liquid subcooling were each chosen to be small enough such that a saturated two-phase flow is observed to develop within a short distance downstream. In this study, the two-phase flow is characterized at a fixed streamwise location for all test conditions, far enough downsteam to ensure that saturated flow boiling conditions exist in the region being visualized. While it would be ideal for the vapor and liquid inlet lines to be maintained exactly at saturation, practical operation of the facility requires some respective degrees of superheat and subcooling to ensure that only single-phase flows enter the T-junction; if the inlet encountered two-phase conditions, the flow periodicity in the test section would be entirely disrupted.

The power levels applied to the test section microchannel were chosen to yield an observable difference in the vapor bubble growth rate over the range. In this study, 13 different input power levels (P_{total}) ranging from 0.32 W to 0.84 W were tested. Two of the power levels (0.32 W and 0.35 W) resulted in condensing flows; the remaining higher power levels (0.40 W to 0.84 W) resulted in evaporating flows. Data were collected for the 13 power levels in a randomized order. The pressure at the outlet of the microchannel measured 105.2 ± 0.8 kPa, which is slightly elevated relative to the ambient pressure due to the flow resistance through the downstream tubing and heat exchanger. The higher power levels might be expected to result in a higher pressure drop across the microchannel (due to a higher evaporation-induced accelerational pressure drop); however, the range of power levels considered in this study is relatively small and thus minimal pressure drop increase was observed across the range. A steady-state condition was allowed to be reached at each successive power level before flow visualization images were obtained using the high-speed camera.

2.3 Flow Visualization

The flow was visualized using a high-speed camera (FASTCAM 1024 PCI, Photron) and two alternative lenses: a macro lens (AF Micro-Nikkor, Nikon) and a high-magnification zoom lens (VH-Z50L, Keyence). The camera and lens assembly was positioned using a three-axis stage and focused on the microchannel mid-plane. The microchannel length was uniformly backlit using an adjustable, high-intensity LED strip with an integrated light diffuser (BL138, Advanced Illumination).

Images obtained using the macro lens were acquired at 27,000 frames per second with an exposure time of 0.037 ms for a duration of 0.74 s at each power level. An image size of 1024 × 32 was used to visualize the high-aspect ratio microchannel geometry. Images collected with the macro lens had an image resolution of 32 μm per pixel, as determined using a calibration target (59217, Edmund Optics), resulting in an optical magnification of 0.5×. The field of view observed with the macro lens was positioned at $98 < y/D < 162$; the beginning of the heated region was $y/D = 92$. The entire vapor-liquid interface profile of several vapor bubbles could be visualized simultaneously within this field of view.

Images acquired using the high-magnification zoom lens were obtained at an image size of 1024 × 512 and resolution of 1.5 μm per pixel (optical magnification of 11.3×). The frame rate was reduced to 2,000 frames per second (with an exposure time of 0.5 ms) to ensure adequate backlighting. The high-magnification lens was used to measure the position of the vapor-liquid interface relative to the inside wall of the microchannel (*i.e.*, the liquid film thickness).

2.4 Image Analysis

Qualitative observations of the vapor-bubble interface were made using the images obtained with the macro lens. The images were analyzed frame-by-frame to characterize the vapor bubble and liquid slug lengths. These lengths were determined from the initial gray-scale images using a custom image-processing algorithm, as shown in Fig. 3. The algorithm subtracts the original image (Fig. 3a) from a background image (Fig. 3b) to generate an image of the vapor-liquid interface profile with enhanced contrast (Fig. 3c). A gray-scale intensity histogram of the resulting image was generated, which had a bimodal distribution; the minimum point between the two peaks was selected as the thresholding value. The gray-scale image was then thresholded to yield a binary image (Fig. 3d). Vapor bubbles featuring an incomplete vapor-liquid interface profile were then removed (Fig. 3e). Finally, the interior of the vapor-liquid interface profiles are filled for easier visual study, resulting in a final image that can be used for extraction of the vapor bubble and liquid slug lengths (Fig. 3f). Feature recognition was used to track each vapor bubble and liquid slug from frame to frame and identify new vapor bubbles entering the camera field of view.

The length of each vapor bubble was determined from the difference between the furthest downstream (*i.e.*, nose) and upstream (*i.e.*, tail) axial locations of the vapor-liquid interface. The liquid slug length was determined from the difference between the tail of a leading vapor bubble and the nose of a trailing vapor bubble. Optical distortions caused by the refraction of light passing through the liquid-solid interface and the gas-solid interface (*i.e.*, air-glass) need not be corrected when measuring the vapor bubble and liquid slug length because the liquid-solid and gas-solid interfaces at the centerline of the microchannel are normal to the camera.

2.5 Liquid Film Thickness

Liquid film thickness is an important parameter in the characterization of two-phase flows, resulting in significant effort having been directed toward predictive correlations and improved measurement techniques [2, 26]. While sophisticated experimental techniques involving laser focus displacement meters [27, 28] and optical microscopes paired with pulsed-laser illumination [29] have been used for high-fidelity characterization of the liquid film interface profile, the flow visualizations obtained via high-speed imaging herein can also yield a film thickness measurement. The thickness of the liquid film separating the vapor bubble from the inside microchannel wall was quantified using the images obtained with the high-magnification zoom lens. The measurement of this liquid film thickness accounts for the optical distortions in the images; a schematic diagram illustrating the optical distortions caused by the liquid-solid and gas-solid interfaces is shown in Fig. 4. To illustrate the relationship between the image and physical interface locations, a quarter section of the microchannel cross-section is shown side-by-side with an image obtained using high-speed imaging, aligned at the channel centerline. Key locations along the interfaces are marked with dots; outward pointing arrows indicate the direction normal to the interfaces at these locations. The dotted lines represent the pathlines of light collected by the high-speed camera from the points of interest at the microchannel *y*-*z* mid-plane; the dashed lines show the *x*- and *z*-positions where the light is refracted along these pathlines.

A ray-tracing procedure was used to transform the *z*-positions of the microchannel inside diameter (z_5) and the vapor-liquid interface (z_6) observed in the image to the actual physical positions of these two interfaces in space (z_2 and z_1, respectively). The procedure assumes the liquid film thickness to be uniform around the microchannel circumference. The dominance of surface tension forces relative to body forces, as indicated by a Bond number of $Bo = 0.24 < 1$,

justifies this assumption. The vapor-liquid interface intersects the microchannel *x-y* mid-plane at the top of a dark band in the image shown Fig. 4; this vapor-liquid interface was used for the ray-tracing procedure. This dark region observed below the mid-plane vapor-liquid interface location is a result of the light being refracted by a region of the foreground/background interface. The location of the microchannel inside diameter is difficult to observe, but is made detectable using image-enhancement techniques. The relationship between the angle of incidence and refraction of the light traversing through the liquid-solid and gas-solid interfaces is given by Snell's Law: $n_a \sin\theta_a = n_b \sin\theta_b$, where n is the index of refraction of the medium and θ is the angle between the normal and the incident/refracted light. The refractive indices of HFE-7100 liquid, borosilicate glass, and air are 1.27, 1.47, and 1.00, respectively.

3 Results and Discussion

3.1 Heat Loss Analysis

A portion of the total power supplied to the ITO coating on the microchannel outer surface is lost to the ambient (*i.e.*, not transferred to the flow through the microchannel wall). Any energy supplied to (removed from) a saturated two-phase flow would change the vapor quality and thus be observed as a streamwise increase (decrease) in the vapor bubble size. Under adiabatic conditions, the size of the vapor bubbles would remain constant. The heat loss to the ambient was quantified by measuring the nondimensional change in vapor bubble length, $\Delta L_b/D$, over a given period of time, for each of the 13 power levels, to identify the power level at which no net evaporation or condensation was occurring. The nondimensional change in vapor bubble length for the 13 different power levels is plotted in Fig. 5 with error bars indicating one standard deviation. A zero net change in nondimensional vapor bubble length, as determined from the

linear regression line, occurs at a power input of 0.39 ± 0.01 W. Because this power input level results in no change in the vapor bubble length, it is deemed to be all lost to the ambient. Hence, the power loss to the ambient, P_{loss} = 0.39 ± 0.01 W; the uncertainty in P_{loss} was quantified based on the uncertainty in the linear regression [30]. For the range of power levels considered in this study, a linear relationship between total power and nondimensional change in vapor bubble length was observed (R^2 = 0.98); hence, the power input to the microchannel, P_{in}, in each case was determined by subtracting the power loss from the total power.

The heat flux into the fluid is $q'' = P_{in}/A_s$, where A_s is the internal surface area of the microchannel. The uncertainty in P_{in} has contributions from uncertainties in the heat loss determined via linear regression and the total power measurement. The uncertainty in A_s has contributions from the uncertainties in the microchannel inside diameter (± 4 μm) and the distance between the electrical connections on the ITO layer (± 1 mm). The resultant propagated uncertainty in the heat flux increases slightly from 150 to 190 W/m^2 over the range of evaporating heat fluxes from 30 to 5160 W/m^2. The large relative uncertainty at q'' = 30 W/m^2 is attributed to the small difference between the total power and the heat loss at this test condition.

3.2 Qualitative Flow Visualizations

Selected images from high-speed visualization of the test section microchannel at heat fluxes of q'' = 30 W/m^2 and q'' = 3520 W/m^2 are shown in Fig. 6. The sequence of frames at each heat flux shows the left-most vapor bubble (in the first frame) traverse the length of the microchannel until it almost begins to exit the camera field-of-view. Visualization of the

evaporating two-phase slug flow allows several important qualitative features to be identified for the inlet conditions of this study:

i. the vapor bubble nose is hemispherical while the tail is much flatter;
ii. the liquid film between the vapor bubble and the microchannel wall slightly reduces along the length of the vapor bubbles beginning at the nose and progressing toward the tail;
iii. the interface at the trailing edge of the vapor bubble fluctuates in time as a result of the recirculation in the wake of the vapor bubble;
iv. capillary waves are observed on the vapor-liquid interface where the liquid film is thinnest;
v. vapor bubbles elongate in time as they evaporate due to the uniform heat flux condition;
vi. longer vapor bubbles elongate at a faster rate than shorter ones as a result of their increased vapor-liquid interfacial surface area;
vii. vapor bubble growth only occurs in the streamwise direction because the vapor bubbles are confined in circumferential extent by the microchannel wall;
viii. the variation in length between successive vapor bubbles is small, as it is for the liquid slugs;
ix. the initial length of the liquid slugs is slightly larger than the initial length of the vapor bubbles;
x. the length of the liquid slugs does not noticeably change as a function of axial position along the microchannel;

xi. flow-regime transitions (*e.g.*, slug to annular) and flow instabilties (*e.g.*, flow reversal) are not observed;

xii. there are no instances of vapor bubble coalesence; and

xiii. there is no nucleation of vapor bubbles from the microchannel wall.

Qualitative differences between Fig. 6a and 6b due to the different heat fluxes applied can also be observed. The vapor bubbles in Fig. 6a elongate at a much slower rate than those in Fig. 6b as a result of the reduced heat flux and the lower associated rate of evaporation. Also, the time required for a vapor bubble in Fig. 6a to translate a given distance downstream is longer than in Fig. 6b (note the additional frame in Fig. 6a). An increased evaporation rate results in an increased acceleration of the flow due to volumetric expansion associated with phase change from liquid to vapor.

To further illustrate the controlled nature of the slug flow generation methodology developed in this work, alternative images from high-speed visualization of vapor bubbles being generated by nucleation from the wall within a heated microchannel and the downstream slug flow regime in this case are shown in Fig. 7. Vast differences in the hydrodynamics are observed for this flow regime generated using an approach where preheated single-phase liquid entered the heated channel and was allowed to nucleate.

3.3 Quantitative Characterization

3.3.1 Vapor Bubble and Liquid Slug Uniformity

The uniformity of the vapor bubble and liquid slug lengths was quantitatively assessed from the images obtained for the evaporating flow test cases (*i.e.*, a positive net heat flux to the microchannel). The initial lengths of the vapor bubbles were measured when the entire vapor-

liquid interface profile first comes into view. This occurs at a fixed vapor bubble tail location of $y'/D = 0.06$, where y' is the axial position along the microchannel beginning at the upstream end of the camera field-of-view; this ensured that a liquid region could be clearly observed at $y'/D = 0$. Similarily, the initial liquid slug length was measured once the entire liquid slug could be observed. The average initial vapor bubble and liquid slug lengths for each heat flux are shown in Fig. 8a. The error bars represent one standard deviation for all of the vapor bubbles and liquid slugs that were analyzed. Histograms illustrating the lengths of each vapor bubble and liquid slug that were observed at a heat flux of $q'' = 3520$ W/m^2 are shown in Fig. 8b and 8c, respectively. The histograms indicate a generally normal distribution with no outliers. The average initial length of the liquid slugs ($L_0/D = 6.8$) is longer than the average initial length of the vapor bubbles ($L_0/D = 4.6$). An average of 113 vapor bubbles was observed over the 0.74 s aquisition period. The average standard deviation in the length of the liquid slugs ($L_0/D = 0.9$) is smaller than the average standard deviation in the length of the vapor bubbles ($L_0/D = 1.1$). This less consistent vapor bubble length results from minuscule variations in flow conditions (*e.g.*, inlet temperatures) that perferentially magnify vapor bubble characteristics relative to the liquid slugs because of the high liquid to vapor density and specific heat ratios.

An ideal slug flow regime for the purpose of validating mechanistic models should feature liquid slug lengths that are large enough to prevent vapor bubble coalescence and a subsequent transition from slug to annular flow. Likewise, the liquid slug length must not be so long that the flow regime is essentially that of single-phase liquid flow with isolated vapor bubbles present. The ability to produce a slug flow regime that resembles archetypal microchannel slug flow by independently injecting vapor and liquid thereby removing a reliance on nucleation from the microchannel wall is unique to this test facility and, to the authors'

knowledge, is the only such demonstration in the literature for a single-component, two-phase diabatic flow.

The range in the average initial vapor bubble length across the different heat fluxes is relatively small (L_0/D = 0.9), being less than one standard deviation in the average vapor bubble length. This small variation confirms that the slightly increased pressure drop across the microchannel at the higher heat fluxes does not result in significant changes in the vapor flow rate through the vapor flow control valve. The vapor flow control valve relies on a pressure difference upstream and downstream of the control valve, unlike the the liquid flow controller, which employs active feedback to regulate the flow rate.

3.3.2 Local Velocity Evaluation

The accelerating flow resulting from evaporation yields a unique velocity at each axial location and requires the flow characteristics to be quantified locally. The average vapor bubble velocity was computed by determining the velocity of each vapor bubble and then averaging across all vapor bubbles at a given heat flux. The velocity was measured by determining the change in axial position and time between the first and last detection point of the vapor bubble in the camera field of view; the midpoint between the vapor bubble nose and tail was used as the axial detection point. A corresponding average Reynolds number, $\mathrm{Re}_D = \overline{V_b} D/\nu_l$, was calculated using the vapor bubble velocity, following prior practice for microchannel slug flow in the literature [28]. The average vapor bubble velocity and Reynolds number for four selected heat fluxes are shown in Table 1.

3.3.3 Film Thickness Quantification

The liquid film thickenss was measured using the high-magnification zoom lens at the heat flux of 3520 W/m^2 as described in Section 2.5. While the thickness of the liquid film is

known to depend on the vapor bubble velocity, only minor changes in velocity were observed for the different heat fluxes; thus, only one heat flux condition was analyzed. The ray-tracing procedure described in Section 2.5 yielded the physical *z*-positions of the microchannel inside wall and the vapor-liquid interface to be $z/D = 0.490 \pm 0.008$ and $z/D = 0.416 \pm 0.016$, respectively; the uncertainties represent a propagation of the image resolution and interface location uncertainty (interfaces can be located in the image within ± 1 pixel). A dimensionless liquid film thickness of $\delta/D = 0.074 \pm 0.018$ resulted.

The current approach does not capture the precise axial location at which the film thickness is measured along the vapor bubble relative to its nose or tail. Due to the relatively low frame rate used with the high-magnification zoom lens, the nose and tail of the vapor bubble blur in the images due to rapid translation of the interface across the field of view in the axial direction. For the average vapor bubble velocity of 0.93 m/s, the vapor-liquid interface translates 0.93D (30% of the image width) during the 0.5 ms exposure time. The interface is therefore visualized in the middle region of the bubble over which the film thickness is approximately constant (along the axial direction); image blur is not observed because the interface appears stationary within the exposure time.

3.3.4 Vapor Bubble Growth

The growth of individual vapor bubbles provides a measure of the evaporation rate. A Lagrangian approach which tracks the growth of individual vapor bubbles with time was chosen. The average nondimensional vapor bubble length versus time is shown in Fig. 9 for four selected heat fluxes considered in this study. The minimum and maximum heat flux levels (q'' = 30 W/m^2 and q'' = 5160 W/m^2, respectively) and two intermediate heat flux levels (q'' = 1250 W/m^2 and q'' = 3520 W/m^2) are included; the other intermediate heat fluxes have

been left out of Fig. 9 for clarity. The error bars represent one standard deviation in the nondimensional vapor bubble length for all of the vapor bubbles analyzed at a given heat flux. The lengths were measured in each frame (at 0.037 ms increments); these high-resolution data are shown as lines in Fig. 9. A nondimensional vapor bubble length of $L_b/D = 5$ was chosen as a common starting length in Fig. 9 because it enabled the most vapor bubbles to be analyzed given that the average initial vapor bubble length was slightly less than $L_b/D = 5$. For a heat flux of $q'' = 30$ W/m^2, a small rate of evaporation results in an average elongation of the vapor bubbles from $L_b/D = 5$ to $L_b/D = 5.2$ in 18 ms. At the highest heat flux of $q'' = 5160$ W/m^2, a much larger evaporation rate elongates the vapor bubble to $L_b/D = 10.7$ over this same period. The intermediate heat flux levels of $q'' = 1250$ W/m^2 and $q'' = 3520$ W/m^2 resulted in vapor bubble lengths elongating to $L_b/D = 6.8$ and $L_b/D = 8.7$, respectively. The vapor bubble growth is monotonic with heat flux for all test cases.

To evaluate the dependence of the growth rate on the vapor bubble length, a second-order polynomial trendline was first fit to the vapor bubble length versus time data for each heat flux; all trendlines had $R^2 > 0.99$. The polynomial was differentiated with respect to time to yield the time rate of change of the average nondimensional vapor bubble length and then plotted against the average nondimensional vapor bubble length (Fig. 10). As shown, the time rate of change in length is higher for higher heat fluxes and increases with increasing vapor bubble length (*i.e.*, evaporation rate increases with a larger interfacial area).

4 Conclusions

An archetypal microchannel slug flow boiling regime was generated by independently injecting HFE-7100 vapor and liquid into a T-junction using a novel experimental test facility.

This approach does not rely on nucleation from the microchannel wall to generate the vapor phase, thereby eliminating flow instabilties, flow-regime transitions, and undesirably close proximity of successive vapor bubbles to each other. The two-phase flow was subjected to a constant heat flux ranging from 30 W/m^2 to 5160 W/m^2. High-speed flow visualization was used to quantitatively characterize the vapor bubble and liquid slug uniformity and vapor bubble growth. High-magnification imaging was demonstrated for quantifying the liquid film thickness using a ray-tracing procedure to account for optical distortions. This study provides a foundation for experimental investigation of microchannel slug flow boiling under conditions suitable for model validation.

Appendix A. Supplementary Data

Supplementary data associated with this article can be found in the online version.

References

[1] C.T. Crowe, J.D. Schwarzkopf, M. Sommerfeld, Y. Tsuji, Multiphase flows with droplets and particles, Taylor & Francis Group, 2011.

[2] R. Gupta, D. Fletcher, B. Haynes, Taylor flow in microchannels: A review of experimental and computational work, The Journal of Computational Multiphase Flows, 2(1) (2010) 1-32.

[3] M. Magnini, J.R. Thome, Computational study of saturated flow boiling within a microchannel in the slug flow regime, Journal of Heat Transfer, 138(2) (2015) 021502.

[4] P. Angeli, A. Gavriilidis, Hydrodynamics of Taylor flow in small channels: A review, Proceedings of the ASME Institution of Mechanical Engineers, Part C: Journal of Mechanical Engineering Science, 222(5) (2008) 737-751.

[5] M.T. Kreutzer, F. Kapteijn, J.A. Moulijn, J.J. Heiszwolf, Multiphase monolith reactors: Chemical reaction engineering of segmented flow in microchannels, Chemical Engineering Science, 60(22) (2005) 5895-5916.

[6] S.G. Kandlikar, Heat transfer and fluid flow in minichannels and microchannels, Elsevier, 2006.

[7] S.V. Garimella, T. Harirchian, Microchannel heat sinks for electronics cooling, in: A. Bar-Cohen (Ed.), Encyclopedia of thermal packaging - thermal packaging techniques, 2013, World Scientific Publishing Company.

[8] J.R. Thome, V. Dupont, A.M. Jacobi, Heat transfer model for evaporation in microchannels. Part I: Presentation of the model, International Journal of Heat and Mass Transfer, 47 (2004) 3375-3385.

[9] T. Harirchian, S.V. Garimella, The critical role of channel cross-sectional area in microchannel flow boiling heat transfer, International Journal of Multiphase Flow, 35(10) (2009) 904-913.

[10] Y.P. Peles, L.P. Yarin, G. Hetsroni, Steady and unsteady flow in a heated capillary, International Journal of Multiphase Flow, 27(4) (2001) 577-598.

[11] A.M. Jacobi, J.R. Thome, Heat transfer model for evaporation of elongated bubble flows in microchannels, Journal of Heat Transfer, 124(6) (2002) 1131-1136.

[12] T. Harirchian, S.V. Garimella, Flow regime-based modeling of heat transfer and pressure drop in microchannel flow boiling, International Journal of Heat and Mass Transfer, 55(4) (2012) 1246-1260.

[13] G. Wang, L. Hao, P. Cheng, A four-zone model for saturated flow boiling in a microchannel of rectangular cross-section, International Journal of Heat and Mass Transfer, 53 (2010) 3439-3448.

[14] A. Esmaeeli, G. Tryggvason, Computations of film boiling. Part I: Numerical method, International Journal of Heat and Mass Transfer, 47(25) (2004) 5451-5461.

[15] D. Sun, J. Xu, Q. Chen, Modeling of the evaporation and condensation phase-change problems with FLUENT, Numerical Heat Transfer, Part B: Fundamentals, 66(4) (2014) 326-342.

[16] M. Magnini, B. Pulvirenti, J.R. Thome, Numerical investigation of hydrodynamics and heat transfer of elongated bubbles during flow boiling in a microchannel, International Journal of Heat and Mass Transfer, 59 (2013) 451-471.

[17] Z. Pan, J.A. Weibel, S.V. Garimella, A saturated-interface-volume phase change model for simulating flow boiling, International Journal of Heat and Mass Transfer, 93 (2016) 945-956.

[18] Y. Tsui, S. Lin, Y. Lai, F. Wu, Phase change calculations for film boiling flows, International Journal of Heat and Mass Transfer, 70 (2014) 745-757.

[19] Z. Pan, J.A. Weibel, S.V. Garimella, Spurious current suppression in VOF-CSF simulation of slug flow through small channels, Numerical Heat Transfer, Part A: Applications, 67(1) (2015) 1-12.

[20] M. Magnini, B. Pulvirenti, J.R. Thome, Numerical investigation of the influence of leading and sequential bubbles on slug flow boiling within a microchannel, International Journal of Thermal Sciences, 71 (2013) 36-52.

[21] C. Kunkelmann, P. Stephan, CFD simulation of boiling flows using the volume-of-fluid method within OpenFOAM, Numerical Heat Transfer, Part A: Applications, 56(8) (2009) 631-646.

[22] S. Hardt, F. Wondra, Evaporation model for interfacial flows based on a continuum-field representation of the source terms, Journal of Computational Physics, 227(11) (2008) 5871-5895.

[23] S. Bigham, S. Moghaddam, Microscale study of mechanisms of heat transfer during flow boiling in a microchannel, International Journal of Heat and Mass Transfer, 88 (2015) 111-121.

[24] A. Scammell, J. Kim, Heat transfer and flow characteristics of rising Taylor bubbles, International Journal of Heat and Mass Transfer, 89 (2015) 379-389.

[25] K. Miyabayashi, O. Tonomura, S. Hasebe, Estimation of gas and liquid slug lengths for T-shaped microreactors, Chemical Engineering Journal, 262 (2015) 1137-1143.

[26] C.B. Tibiriçá, F.J. do Nascimento, G. Ribatski, Film thickness measurement techniques applied to micro-scale two-phase flow systems, Experimental Thermal and Fluid Science, 34(4) (2010) 463-473.

[27] Y. Han, N. Shikazono, Measurement of liquid film thickness in micro square channel, International Journal of Multiphase Flow, 35(10) (2009) 896-903.

[28] Y. Han, N. Shikazono, Measurement of the liquid film thickness in micro tube slug flow, International Journal of Heat and Fluid Flow, 30(5) (2009) 842-853.

[29] R.S. Patel, J.A. Weibel, S.V. Garimella, An optical approach for quantitative characterization of slug bubble interface profiles in a two-phase microchannel flow, International Journal of Heat and Mass Transfer, 86 (2015) 31-38.

[30] K.K. Brown, H.W. Coleman, W.G. Steele, A methodology for determining experimental uncertainties in regressions, Journal of Fluids Engineering, 120(3) (1998) 445-456.

List of Tables

List of Figures

Fig. 9. The average growth of vapor bubbles, as indicated by the nondimensional vapor bubble length as a function of time, for four heat flux levels. The growth is shown from a common starting bubble length of $L_b/D = 5$.

Fig. 10. The time rate of change of the vapor bubble length as a function of the vapor bubble length for four heat flux levels.

Tables

Table 1. Average vapor bubble velocity and corresponding average Reynolds number.

Heat Flux, q'' [W/m^2]	Average Vapor Bubble Velocity, $\overline{V_b}$ [m/s]	Average Reynolds Number, Re_D [-]
30	0.89	1650
1250	0.91	1690
3520	0.93	1720
5160	0.94	1740

Figures

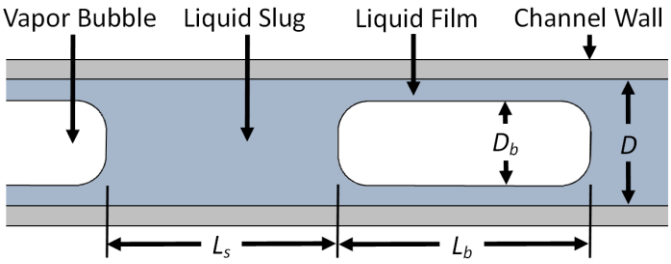

Fig. 1. Schematic diagram illustrating the slug flow boiling regime.

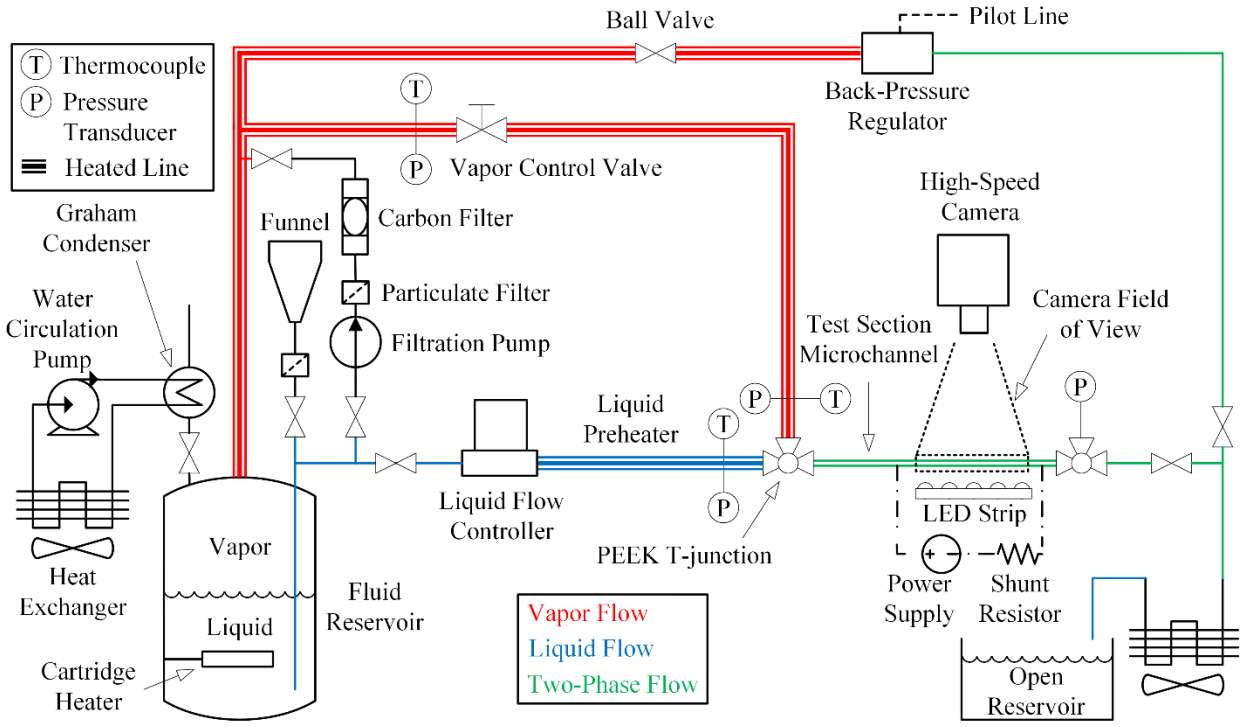

Fig. 2. Schematic diagram of the experimental test facility.

Fig. 3. Selected frame showing the (a) original image, (b) background image, (c) gray-scale image after background subtraction, (d) binary image after thresholding, (e) binary image after removing partial bubble interfaces, and (f) final binary image with vapor bubbles filled in white. The flow direction is from left to right.

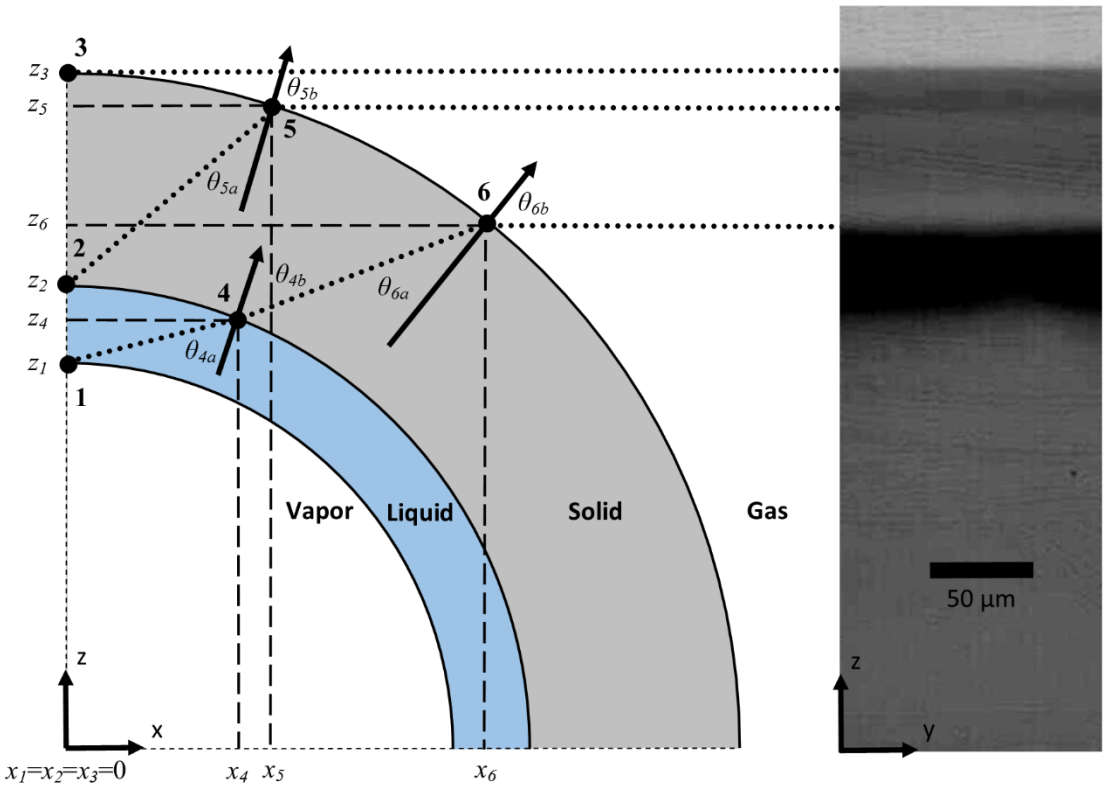

Fig. 4. Schematic diagram illustrating optical distortions caused by the liquid-solid and gas-solid interfaces; the relationship between the image obtained and key physical interface locations is shown.

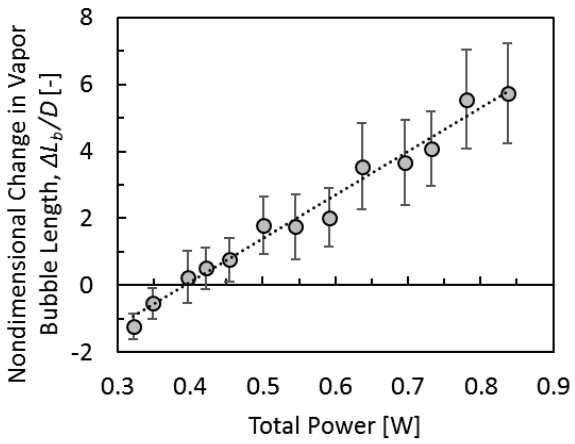

Fig. 5. The nondimensional change in vapor bubble length at varying input powers to the ITO microchannel coating; heat loss to the ambient is quantified as the intercept with the horizontal axis.

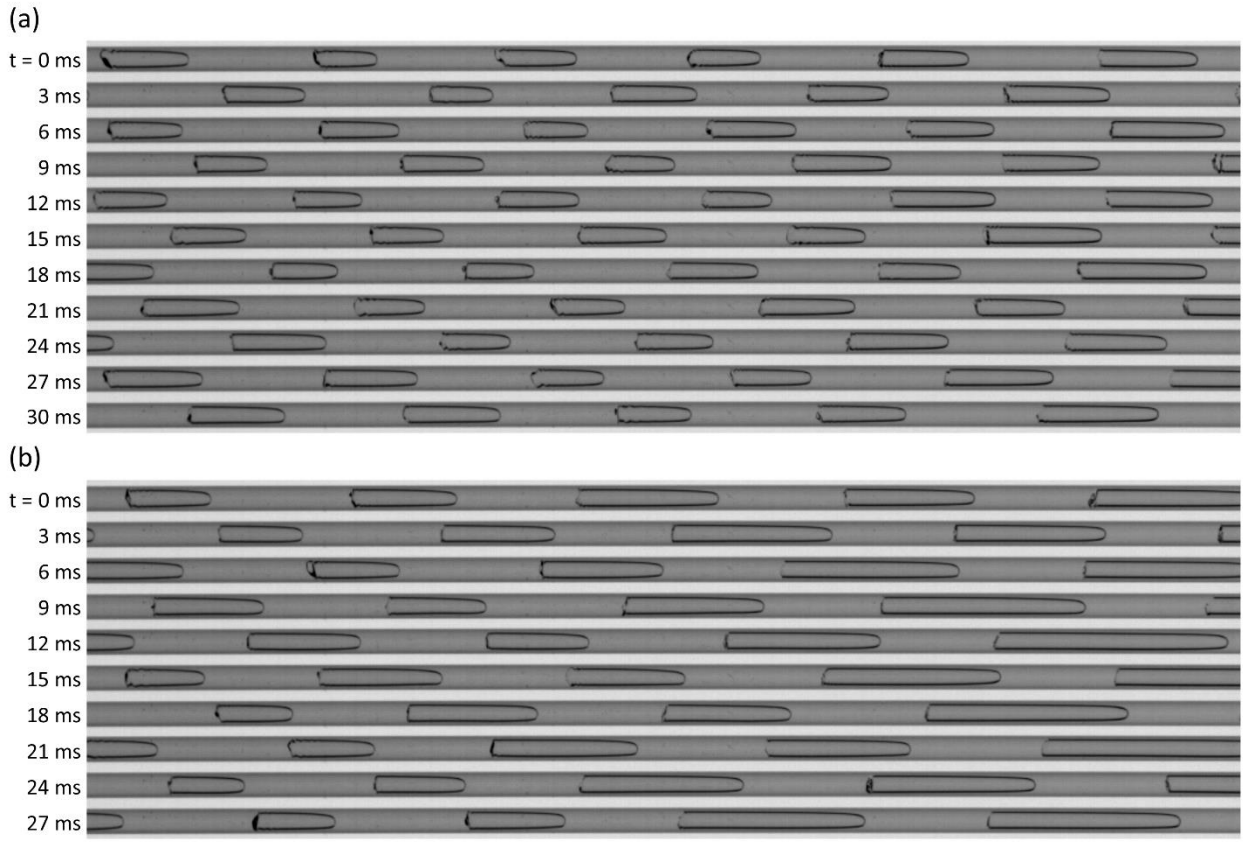

Fig. 6. Selected images at 3 ms increments obtained from high-speed imaging at heat fluxes of (a) q'' = 30 W/m^2 and (b) q'' = 3520 W/m^2 (Supplementary Video 1). The flow direction is from left to right.

Fig. 7. High-speed visualization of (a) vapor bubbles nucleating from a heated microchannel wall and (b) the resulting downstream slug flow.

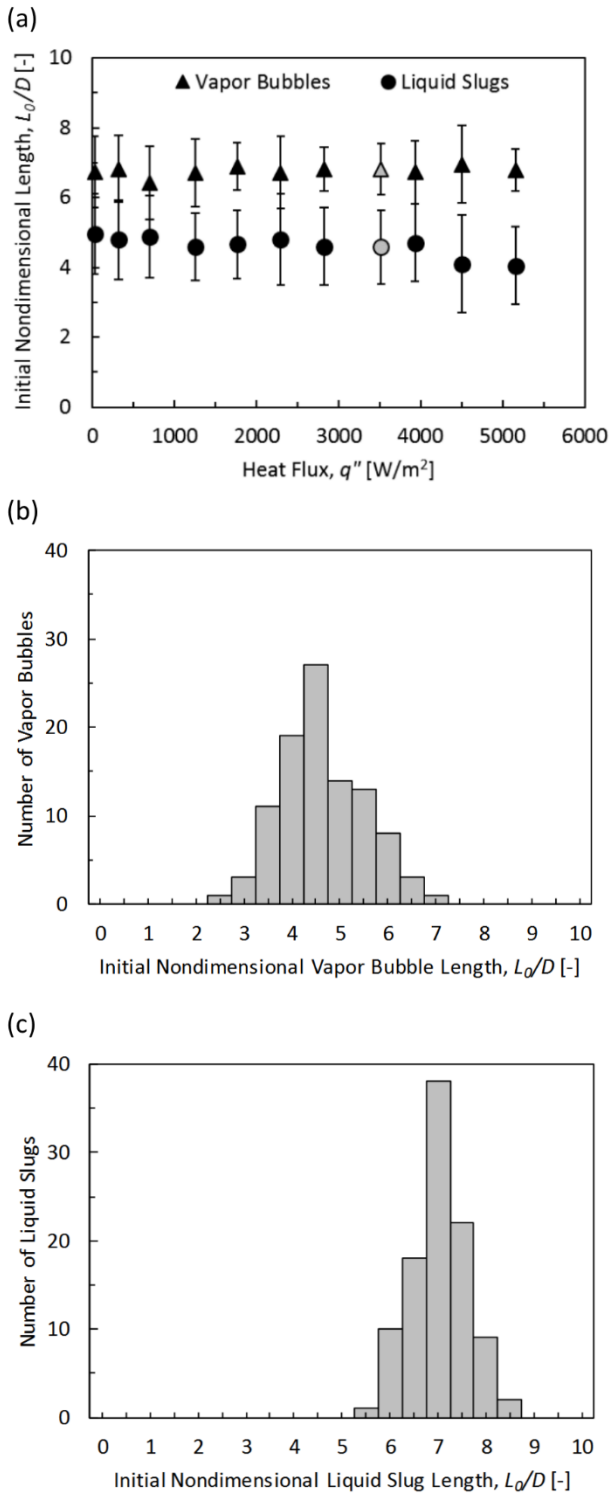

Fig. 8. The (a) average vapor bubble and liquid slug length for each heat flux and histograms of all (b) vapor bubble and (c) liquid slug lengths observed at a heat flux of q'' = 3520 W/m^2 (gray symbols in Fig. 8a).

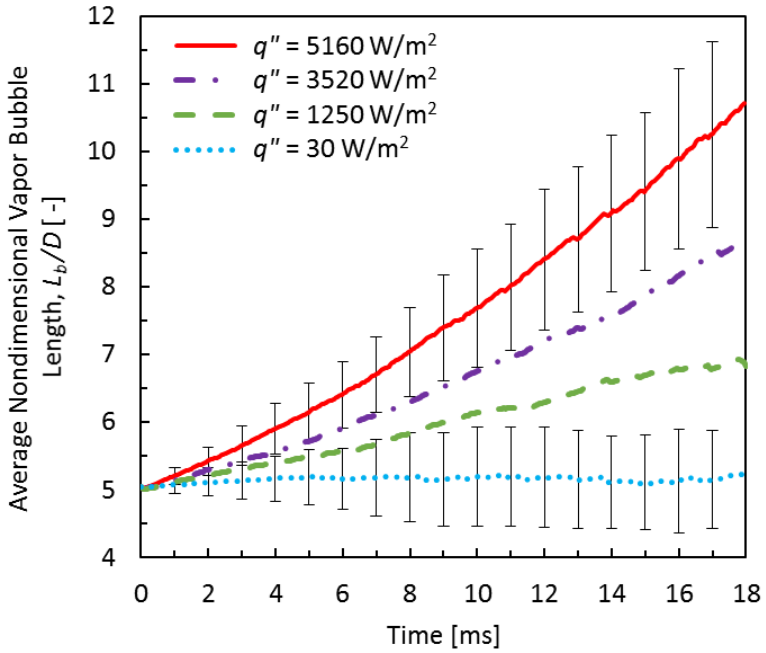

Fig. 9. The average growth of vapor bubbles, as indicated by the nondimensional vapor bubble length as a function of time, for four heat flux levels. The growth is shown from a common starting bubble length of L_b/D = 5.

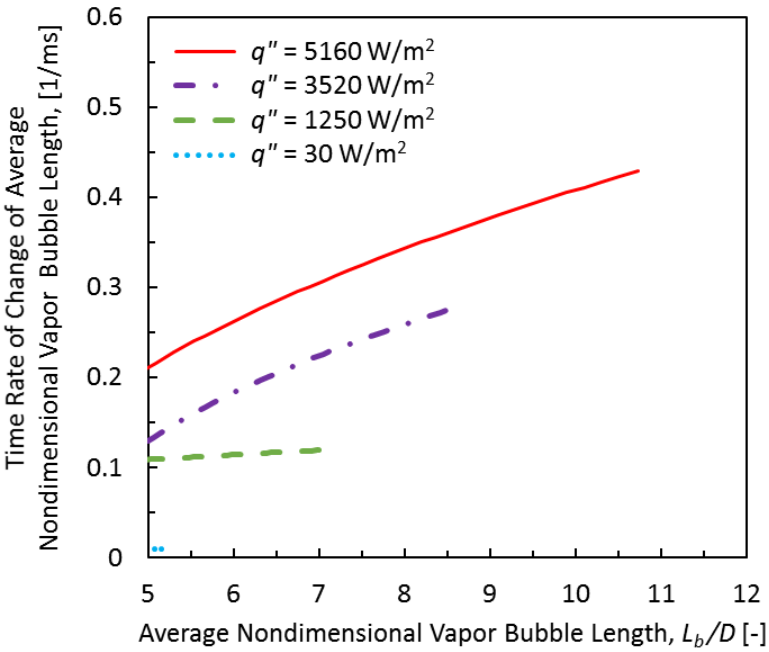

Fig. 10. The time rate of change of the vapor bubble length as a function of the vapor bubble length for four heat flux levels.